AIP | Physics of Fluids

Evolution of turbulence and in-plane vortices in the near field flow behind multi-scale planar grids

L. Gan and P.-Å. Krogstad

Citation: Physics of Fluids **28**, 085101 (2016); doi: 10.1063/1.4960025
View online: http://dx.doi.org/10.1063/1.4960025
View Table of Contents: http://scitation.aip.org/content/aip/journal/pof2/28/8?ver=pdfcov
Published by the AIP Publishing

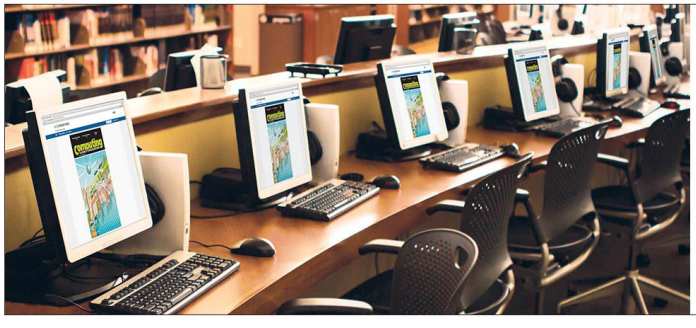

PHYSICS OF FLUIDS **28**, 085101 (2016)

Evolution of turbulence and in-plane vortices in the near field flow behind multi-scale planar grids

L. Gan[1,a)] and P.-Å. Krogstad[2]
[1]*School of Engineering and Computing Sciences, Durham University, Durham, DH1 3LE, United Kingdom*
[2]*Department of Energy and Process Engineering, Norwegian University of Science and Technology, 7491, Trondheim, Norway*

(Received 12 May 2016; accepted 18 July 2016; published online 8 August 2016)

In this experimental work, we carry out detailed two-dimensional particle image velocimetry investigations for the near field wakes behind a conventional and two multi-scale planar grids, using stitched camera fields of view. Statistical independent measurements are conducted focusing on the first few mesh distances downstream of the grid. It is found that the multiple integral length scales originated from the grids loose their importance on the turbulence development after about three mesh distances downstream, much earlier than the distance where the turbulence becomes homogeneous. The largest eddy size, represented by the integral length scales, does not show clear differences in its growth rate among the three grids after an initial development of three times the largest grid size downstream. Nevertheless, when examining individual vortex behaviours using conditional averaging and filtering processes, clear differences are found. The grids are found to have different decay rates of peak vorticity and projected vortex strengths. Despite these differences, the in-plane vorticity correlation function reveals that the mean vortex shape of all the grids shows a universal near-Gaussian pattern which does not change much as the turbulence decays. *Published by AIP Publishing.* [http://dx.doi.org/10.1063/1.4960025]

I. INTRODUCTION

Grid generated turbulence has been the most commonly adopted experimental setup to study the theoretical turbulent flows approaching homogeneous and isotropic conditions. Turbulent flows generated by passive grids have attracted nearly one century of intensive study ever since the first measurement of velocity fluctuations were made.[27] In this respect, the focus has been on the turbulent kinetic energy decay laws in the far field using hot-wire anemometry (HWA) as investigation tools.[3,16,18,19,21]

Compared to the vast amount of experimental investigations in the far field, the region just downstream of the grids, where the flow is highly inhomogeneous and grid geometry dependent, has received considerably less attention until recent years. Batchelor[1] suggested that the near field extends downstream to $x/M \leq 20$, where x is the downstream distance from the grid and M is the size of the repeating unit of the grid. Others, e.g., Corrsin,[7] suggested a broader range, down to $x \approx 40$M. Recent interest in the near field turbulence stems from the findings that the initial conditions may affect the far field turbulence decay.[21] A new exponential decay of turbulence was proposed[16] based on HWA measurements downstream of a space-filling square fractal grid. This is in contrast to the classical power law decay.[26] George[11] indicated that this is an effect of multiple length scales disrupting the energy cascade at higher wave numbers. However, the findings from the measurement in another type of multi-scale grids[19] show that even though the turbulence is originated from the mixing of multiple length scales, the far field decay behaviour is still sufficiently close to the Saffman type.[26] This requires strict homogeneity to be satisfied, which may be the case

a)lian.gan@durham.ac.uk

for $x > 50M$. A near field investigation using laser Doppler anemometry (LDA)[20] found that even though an exponential decay can be observed after the peak turbulence intensity, the range where this applies is rather short and a fit of a classical power law to the data was equally good. The exponent in the inhomogeneous near field region is, however, significantly higher than in the far field in the same flows, where the power law exponent agrees well with the Saffron theory.

Turbulence in the near field, especially right after the grids, is highly three-dimensional. The spatial and temporal development of coherent structures is very complex. There will normally be a considerable recirculation zone behind the grid bars, where strong reversed flows are found. At Reynolds numbers based on M (Re_M) of the order of 10^4, the recirculation zone, determined by the distance from the grid to the apparent stagnation point (if any), may typically extend from $x/M \approx 1$[4] to 1.75[20] depending on the grid geometry. Even though the resolution and signal-to-noise ratio of HWA is much better than most other techniques commonly adopted in turbulence measurements, its limitation of not being able to measure reversed flows makes it an unsuitable tool in regions very close to the grid. For this reason, the lower limit of the applicable downstream distance x for HWA studies is normally $x \approx 1$M,[17] except behind the centre of the hole, where velocity reversal is normally not seen.

In this sense, LDA and particle image velocimetry (PIV) are more suitable candidates to investigate this region. For this study, PIV is preferred, since it gives spatial information at reasonably satisfactory spatial resolution. Using fast cameras and lasers, good temporal resolution can also be achieved as well. The spatial information may be used to derive correlation functions and velocity gradients. This gives unique advantage over point-measurement techniques.

PIV measurements in the near grid region are rare. Cardesa *et al.*[4] studied the flow near bi-plane grids and Gomes-Fernandes *et al.*[12] used monoplane multi-scale grids. In the former study, well converged velocity statistics in the near field of two types of conventional grids are reported. In the latter, multi-resolution PIV experiments were carried out in a mono-plane fractal-geometry grid. A wake-interaction length scale was proposed, which was used to collapse the streamwise fluctuating velocity. Investigations on the wake from this particular fractal grid were extended to a stereoscopic PIV study on the evolution of the completed velocity-gradient tensor, which was available using the frozen turbulence assumption (Taylor's hypothesis).[13] Also a two-dimensional particle image velocimetry (2DPIV) study of the energy transfer in the very near field, where the turbulence is highly inhomogeneous and anisotropic, was made.[14] Other examples include a recent tomographic PIV investigation[9] and a combined PIV and LDA study of the near field in shallow water grid turbulence.[29]

It is also worth mentioning some recent HWA measurements in the near field of multi-scale grids, including studies of turbulence energy decay,[15,28] which verify the power-law decay rate in the near and far fields for static and dynamic grids, respectively. In terms of near field grid turbulence, some examples of DNS studies must be acknowledged,[8,10,22] although their Reynolds numbers are limited, typically one order of magnitude smaller than those in the experiments.

This work is inspired by the near field PIV study of bi-plane grid turbulence by Cardesa *et al.*[4] and builds on the LDA measurements of Krogstad and Davidson.[20] We carry out statistically independent two dimensional 2DPIV investigations in the near field turbulent wake generated by a conventional and two multi-scale planar grids. Our interest is particularly in the evolution of conventional turbulence quantities in the immediate vicinity of the grids and the observed in-plane vortex packets.

II. EXPERIMENTAL SETUP

The experiment was conducted in the facility previously reported by Cardesa *et al.*[4] This water channel is made of 10 mm thick perspex and has an 8 m long working section with a 0.9×0.5 m^2 cross section. Three mono-plane grids made of 2 mm thick stainless steel were installed at the entrance of the working section. Grid 1 was of conventional type (denoted as CONV) with regular repeated square holes of 28.1 mm separated by 9.4 mm wide bars. Grids 2 and 3 were the multi-scale grids (denoted as MSG1 and MSG2) shown in Figure 1. These grids are similar

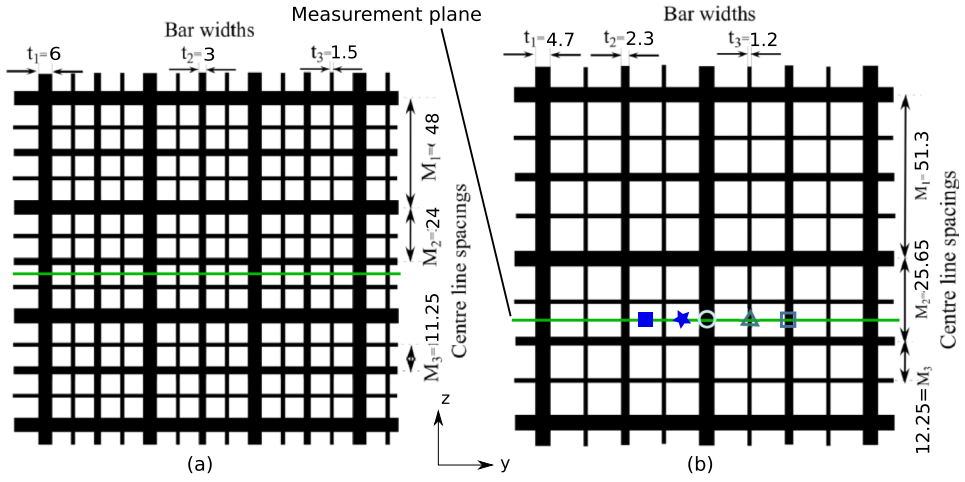

FIG. 1. The two multi-scale grids studied, with the measurement planes shown in green. (a) MSG1; (b) MSG2. The starting point of five characteristic lines in the measurement plane for these grids are indicated by: ○: behind the thickest bar (B1); □: the medium bar (B2); △: the thinnest bar (B3); ★: (H1) centre of the hole beside B1; ■: (H2) centre of the hole beside B2. There are only two similar characteristic lines for the conventional grid, starting at the centre of the hole (H) and behind the middle of the vertical bars (B). These are also the starting points of the characteristic symmetry lines in the streamwise direction. (The conventional grid is not shown.).

to the ones adopted in the LDA measurements of Krogstad and Davidson,[20] with the repeating pattern size, M_1, being 37.5 mm for CONV, 48 mm for MSG1 and 51.3 mm for MSG2, respectively. The solidity ratios (blockage ratios) were $\sigma \approx 44\%$, 44% and 33%. Other important ratio, the size of the thinnest bar to the width of the smallest hole, which we define here as ζ, were 33.45%, 16.67% and 11.43%, respectively. In order to make direct comparison with the turbulent flow behind the bi-plane grids of Cardesa *et al.*,[4] the water channel was operated at the free stream velocity of $U_\infty = 0.5 \pm 0.02$ ms^{-1}, producing a Reynolds number based on M_1 of CONV of $Re_{M1} = U_\infty M_1/\nu = 18\,750 \pm 750$. This gave $\mathrm{Re}_\lambda \sim 840$ measured at $x \approx 1M_1$ downstream of the bar, which was the streamwise position where the streamwise fluctuation velocity was at its maximum. Here $Re_\lambda = u'\lambda/\nu$ and $\lambda = \sqrt{\langle u^2\rangle/\langle(\partial u/\partial x)^2\rangle}$ is the Taylor microscale; see Sec. III A for the definition of variables.

Our 2D PIV experiments were conducted immediately downstream of the grids and the data were taken in a horizontal plane, i.e., the (x, y) planes shown in Figure 1. Figure 1 also marks the starting points of the characteristic symmetry lines (normal to the grid planes) for the two MSG grids. Their positions are summarised in Table I. The z location of the measurement plane cuts through the centres of the holes in all the three grids. Hence data along lines starting in the wake of all bars were obtained, but no measurements were taken in z planes that pass through the intersection of any bars. In order to extend the field of view (FOV) in the downstream direction to about $10M_1$ while maintaining sufficient spatial resolution, simultaneous data from four Photron SA1 cameras (1024×1024 active pixels at current operation conditions) were stitched in the streamwise

TABLE I. The dimensionless spanwise distance $\Delta y/M_1$ of the characteristic symmetry lines (see Figure 1) from the centre of the repeating unit, i.e., the hole centre of the CONV (H) and the centre of the medium bar (B2) of the MSG grids.

Grids	H1	H2	B1	B2	B3
CONV	0.00 (H)		0.50 (B)		
MSG1	0.34	0.09	0.50	0.00	0.23
MSG2	0.35	0.10	0.50	0.00	0.25

direction. Typical overlaps between neighbouring cameras was 7–8 mm, which corresponds to 7-9 equivalent processed vectors. The four cameras covered a combined FOV of about 160×600 mm^2, along the centre line of the channel. The flow was seeded by silver coated hollow glass spheres of 10 μm, and the FOV was illuminated by a dual-cavity diode pumped Nd:YLF Pegasus laser.

The signal synchronisation was generated by programming a LabView signal generator. The particle images were then processed by LaVision Davis 7 software. The interrogation window size was set to 16×16 pixel^2 with 50% overlap, which gives a spatial resolution based on the interrogation window size of 2.54 mm, and a velocity vector spacing of 1.27 mm. The effect of the interrogation window size on the computed turbulence intensities in a similar flow was discussed in a previous study[4] and found to be satisfactory.

The PIV pulse delay, Δt, was set to 1 ms. In order to keep the data set statistically independent, the sampling rate was set at 2 Hz and the total sampling time was about 24 min. In total 2780 velocity field samples were obtained for each measurement. Figure 2 shows that by 1500 samples, the flow field is approximately statistically converged. The convergence quantity plotted is calculated according to

$$\psi_T = \left\{ \frac{1}{T} \int_{t=0}^{T} \left(\psi_t - \frac{1}{T} \int_{t=0}^{T} \psi_t \mathrm{d}t \right)^2 \mathrm{d}t \right\}^{1/2}, \tag{1}$$

where ψ represents the velocity components u or v; see Sec. III A for their definitions. The data shown in the figure were sampled behind one of the thickest bars, B1, for all grids, at the location where the turbulent energy had a peak.

The assessment of the PIV intrinsic error has been discussed intensively in a number of technical papers, e.g., Norbach.[23] The algorithm used by PIV FFT determines the particle displacement with a typical 0.1 pixel uncertainty. Converted to the average pixel shift by the settings used in this experiment, the uncertainty is estimated to about 3%. The approach proposed by Benedict and Gould[2] is taken to get a quantitative estimation of the measurement uncertainty due to the finite sample size. The uncertainty of measuring a quantity is estimated to be $\pm K\sqrt{S_x/N}$, where S_x/N is the sampling variance of the particular quantity at a sample size N. At 95% confidence interval, K is taken to be 1.96. The expression of the sampling variance S_x/N depends on the quantity measured. Using the mean streamwise velocity U and the normal stresses $\langle u^2 \rangle$ as examples, $S_x/N = \overline{u^2}/N$ and $\left[\overline{u^4} - \left(\overline{u^2}\right)^2\right]/N$, respectively; here u represents the fluctuating component of the streamwise velocity. Similarly to the convergence check in Figure 2, at the locations where the fluctuating strength is at the highest level, the estimated uncertainty $\pm 1.96\sqrt{S_x/N}$ for U and $\langle u^2 \rangle$ ($\langle v^2 \rangle$ being similar) are typically ±2% and ±5%, respectively. It is also quantitatively in line with the bi-plane grid measurements,[4] but at a smaller N.

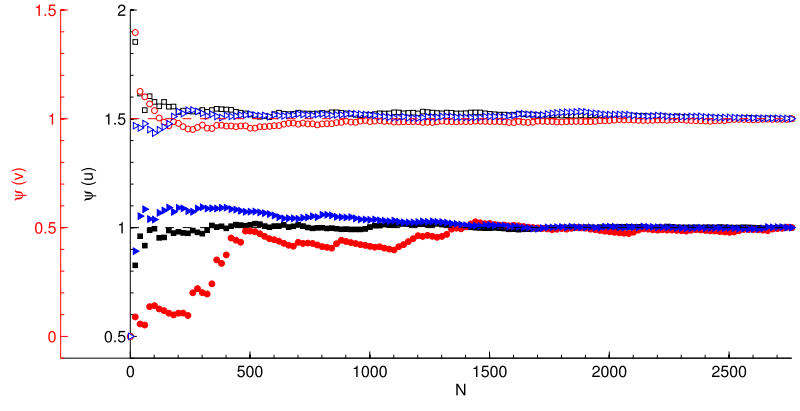

FIG. 2. Convergence history for the two fluctuating velocity components $\psi(u)$ and $\psi(v)$. Data sampled at the location of the strongest fluctuations behind the thickest bar B1. The data are normalised by their final values. ■: CONV; ●: MSG1; ►: MSG2. Filled symbols for the u component and open symbols for v. Only every twentieth data point is shown.

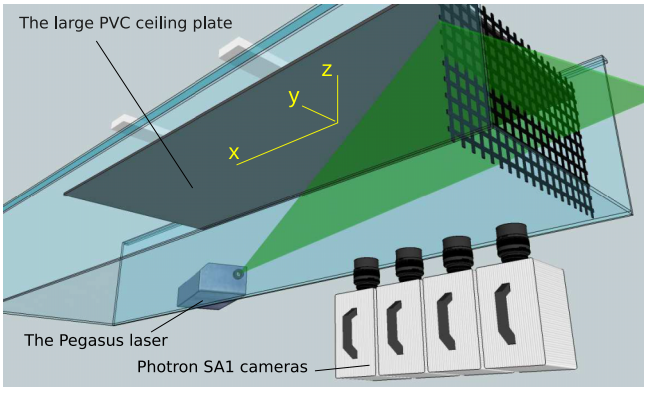

FIG. 3. Sketch of the water channel test section and the PIV arrangement. The large PVC ceiling plate was introduced in order to eliminate free surface effects. The supporting frames for the laser and the cameras are not shown. Flow is from right to left, in the $+x$ direction. (The sketch is not to scale.).

Due to the blockage effect of the grid on the flow, a hydraulic drop forms across the grid at the water free surface. This produces some undesired turbulence and bubbles which can influence the turbulence intensity in the upstream area of the FOV. To reduce this effect, a large ceiling plate made of PVC was installed about 5 cm below the water surface, covering the entire width of the channel. The z coordinate of the measurement plane is half-way between the ceiling plate and the bottom of the channel. Figure 3 presents a sketch of the facility and the PIV measurement system arrangement.

III. EXPERIMENTAL RESULTS

A. The mean velocity

Figure 4 shows a zoomed-in view of the instantaneous 2D vorticity ω_z and velocity vectors in the wake immediately behind the grids. The pattern of the vortex shedding behind the thickest bar is clearly observed and the von Kármán type vortex street can also be noticed behind bar B2 for MSG2 ($y = 0$ mm). The width of the thinnest bar (B3) for the two multi-scale grids is similar to the spatial resolution of the measurements and the vortices shed by B3 could therefore not be well resolved. However, a very weak von Kármán pattern may be seen, e.g., at $y \approx -11$ mm for MSG1 and $y \approx -12.8$ mm for MSG2.

The mean streamwise velocity, U, is shown in Figure 5 for four downstream locations. Here upper case U denotes the ensemble averaged streamwise mean velocity, lower case u is the fluctuating velocity and u' denotes its rms value, u ($u' = \langle u^2 \rangle^{1/2}$). The distribution of the mean in-plane vorticity, $\Omega = (\partial V/\partial x - \partial U/\partial y)$, is given in Figure 6.

Intuitively, one would expect to see a recirculating region immediately behind all vertical bars in the measurement plane. This is evident in the mean velocity profiles for the two MSG grids (Figure 5) in the form of negative U at $x/M = 0.13$ near $y/M \approx \pm 0.5$. However, the velocity for CONV at this station is always positive, so no recirculation appears to exist here. Krogstad and Davidson[20] found that the separated region behind the intersection of the horizontal and vertical bars for this grid was so strong that fluid was drawn in from all sides of the cross, thus eliminating the separated region along the centre plane where the present data were taken.

To confirm this unexpected observation, a Fluent Reynolds-averaged Navier-Stokes (RANS) modelling was undertaken. The modelled grid geometry contained 5×5 repeated units and symmetry boundary conditions were used at two sides and solid wall boundary conditions at the other two, which makes it equivalent to a 10×10 unit grid flow in a closed channel-like configuration. The modelled region covered $16M_1$ in the downstream direction. Both realisable $k-\epsilon$, $k-\omega$ models with various wall functions and different meshing structures were tested. Various coefficient values commonly reported in the literature[30] were also tried. Although the predicted turbulence quantities differed somewhat from the experimental ones, the mean flow was found to be quite insensitive

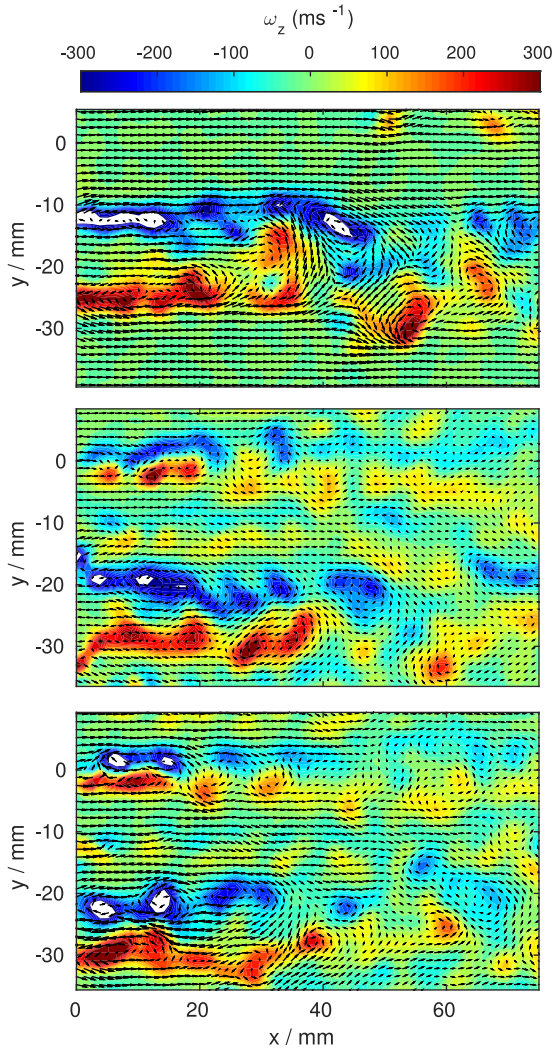

FIG. 4. Part of the instantaneous velocity and vorticity fields immediately downstream of the three grids. The spanwise range shown is about one M for CONV and half M for MSG1 and MSG2. The free stream velocity U_∞ is subtracted from the instantaneous velocities to show the velocity vectors more clearly. From top to bottom: CONV, MSG1, and MSG2.

to the RANS models and the parameter values used. The U profile at $0.13M_1$ downstream of the grid produced from the realizable $k-\epsilon$ model is included in Figures 5 and 6 for comparison. The general trends are the same as in the experiments, confirming that no recirculation zone exists behind the bars of the CONV grid at the symmetry plane.

The situations for MSG1 and MSG2 grids are different. At the measurement plane, the B1 bars are much wider than the adjacent horizontal B2 and B3 bars, hence the influence from the crosses (B1 & B2, B1 & B3) is relatively weak.

The profiles at $0.13M_1$ clearly show that grid CONV has two characteristic symmetry lines, whereas grids MSG1 and MSG2 both have five. This close to the grid, the U_{max} is not along the centre of a hole, but near the edges of the bars, where a strong shear zone is found for all three grids. The velocity overshoot is more obvious in the CONV case and is also supported by the RANS model. The CONV grid has the widest bars and therefore the acceleration around the edges of the bluff body formed by a bar is the strongest. The streamwise development of $U(x)$ along all the characteristic symmetry lines are shown in Figure 7.

Figure 5 also demonstrates the geometry dependence of the velocity distribution between the two multi-scale grids. The maximum velocity of MSG2 (near centre H1 at $|\ y/M_1\ | \approx 0.34$), having

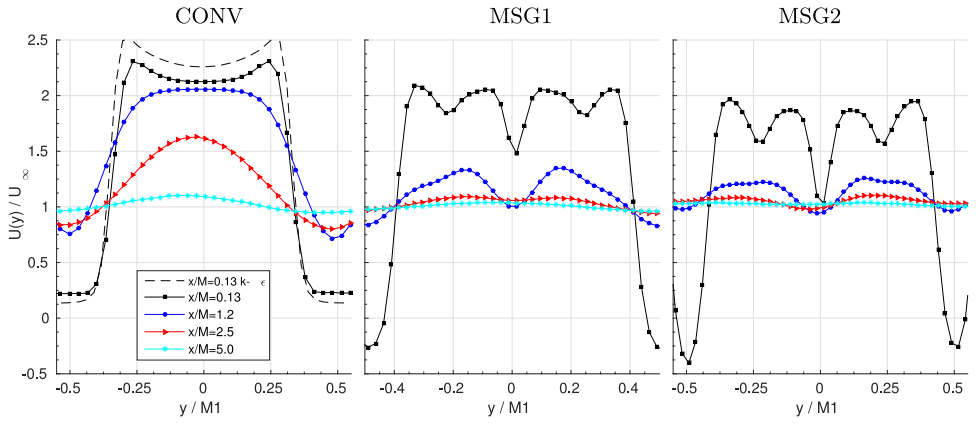

FIG. 5. The spanwise distribution of the mean streamwise velocity component $U(y)$ at downstream locations $x/M_1 = 0.13$, 1.2, 2.5, and 5.0. $U(y)$ is normalised by the free stream velocity U_∞. Only about one period of the spanwise range is presented, from one B1 to the next B1. RANS predictions using the $k-\epsilon$ model is included for CONV at $x/M_1 = 0.13$ (dashed line) for comparison.

the smallest blockage ratio, is slightly lesser than that of MSG1. Due to the longer distances from the bars to its neighbours in MSG2 compared to MSG1, the minimum velocities at $y/M_1 = 0$ and $|\ y/M_1\ | = 0.5$ are lower for MSG2. Figure 7 shows that the peak in U is found within the first $0.2M_1$ downstream of the grid for both MSG grids. But for the CONV grid, the peak occurs at $x \approx 0.5M_1$ downstream of the hole, reaching more than twice the free stream velocity ($U_{max} = 2.4U_\infty$). Beyond the peak, the mean velocity U becomes spanwise homogeneous more quickly for the two MSG grids. At $x/M_1 = 2.5$ there is hardly any y dependence in U (Figure 5), while the spanwise profile for CONV still has a difference by a factor of two between the highest and lowest velocities. Due to the stronger mixing, the mean flow behind the two MSG grids is very complex, i.e., the maximum velocity switches over between the distributions from H1 and H2 twice and can be overtaken by the B3 distribution. Downstream of the MSG2 grid, the minimum velocity also switches between the lines from B1 and B2.

The two MSG grids are geometrically similar, but the different ζ ratios renders the behaviour of U along the two hole centre lines very different. The very small ζ of MSG2 makes the U along the H1 and H2 lines collapse early at $x \approx 0.4M_1$, while for MSG1, the development from H1 is affected by B1 to a larger degree and leads to the H2 distribution approaching U_∞ at the slowest rate among the five characteristic lines (Figure 7).

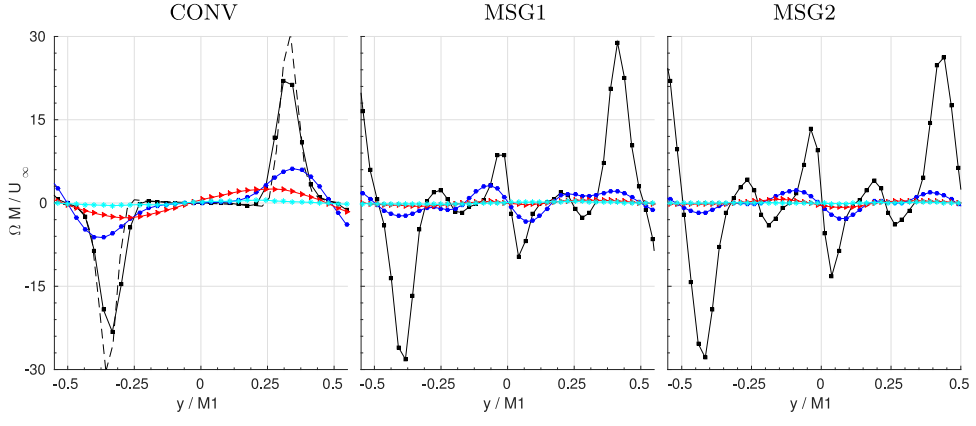

FIG. 6. Spanwise distribution of the in-plane vorticity Ω_z at locations $x/M_1 = 0.13$, 1.2, 2.5, and 5.0. Line definitions as in Figure 5.

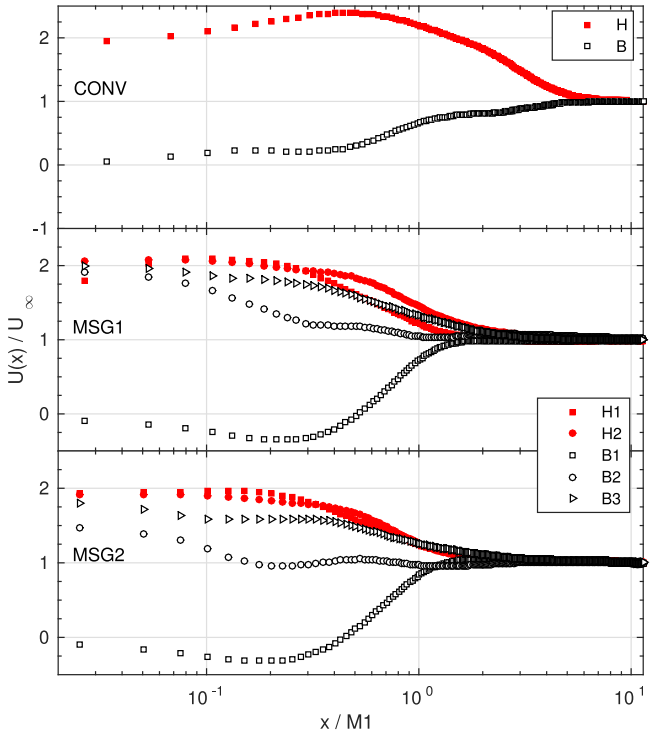

FIG. 7. The streamwise development of the mean streamwise velocity $U(x)$ behind H and B.

B. Turbulent stresses

The streamwise development of the two turbulent stresses measured in this setup, $\langle u^2 \rangle$ and $\langle v^2 \rangle$, along the selected lines is shown in Figures 8 and 9. The following characteristics may be deduced from the figures:

1. Behind bar B of the CONV grid there are double $\langle u^2 \rangle$ peaks with a region of significant stress reduction in between (Figure 8 CONV). This is not observed in the two bi-plane grids of Cardesa *et al*. under similar Re conditions.[4] This range between the primary peak and the valley collapses approximately with the first plateau of U at $0.13 \lesssim x/M_1 \lesssim 0.4$ seen in Figure 7 for B and may be associated with the missing recirculation zone in the mono-plane grid wake.
2. As may be expected, the development of the turbulence in the near region is very complex for all grids when strong mixing takes place. The more complicated the grid geometry is, the

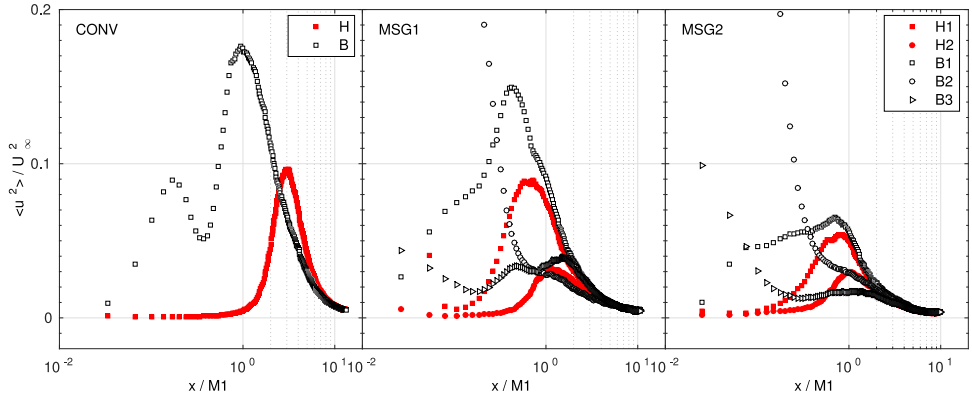

FIG. 8. Development of the normalised streamwise component of Reynolds stress $\langle u^2 \rangle / U_\infty^2$ along the characteristic symmetry lines.

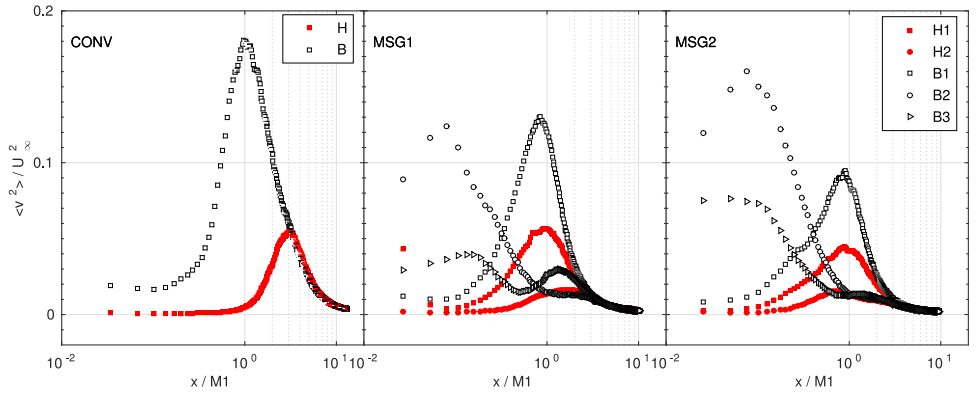

FIG. 9. The normalised spanwise component of Reynolds stress $\langle v^2 \rangle / U_\infty^2$ along the characteristic symmetry lines.

stronger is the interaction between the flows along the different lines. And the interaction takes place at different streamwise positions depending on the spacing and thickness of the bars. The stress behind the thickest bar is generally stronger than that behind a hole for all x. For the CONV grid there is a distinct switch of high turbulent intensity zone from behind bars to behind holes at $x = 2.5M_1$. This occurs as the turbulence generated at the bar decays while new turbulent energy is produced in the strong shear layers formed closer to the hole centre (at about $| y/M_1 | \approx 0.2$ to 0.3 for $x = 2.5M_1$ in Figure 5).

3. There are very high stresses immediately behind B3 and B2 for both MSG grids, being attributed to the vortex shedding at the edges of these bars (see Figure 4). The very strong intensity may be due to the relatively limited spatial resolution there, causing the PIV data at the symmetry line to be contaminated by the vortex shedding from the edges and therefore not being the true symmetry line data behind those bars.

The highest $\langle u^2 \rangle$ in the flow field does not occur along the characteristic lines of the geometry, but within the strong shear regions located a small distance away from these lines. To illustrate this point the spanwise distribution of $\langle u^2 \rangle$ and $\langle v^2 \rangle$ at their peak values on the characteristic lines behind the thickest bar is presented in Figure 10. These peaks are found at $x/M_1 = 1.0, 0.45$, and 0.7 for the CONV, MSG1 and MSG2 grids, respectively, for the u component. For v, the positions are at $x/M_1 = 1.0, 0.85$, and 0.9.

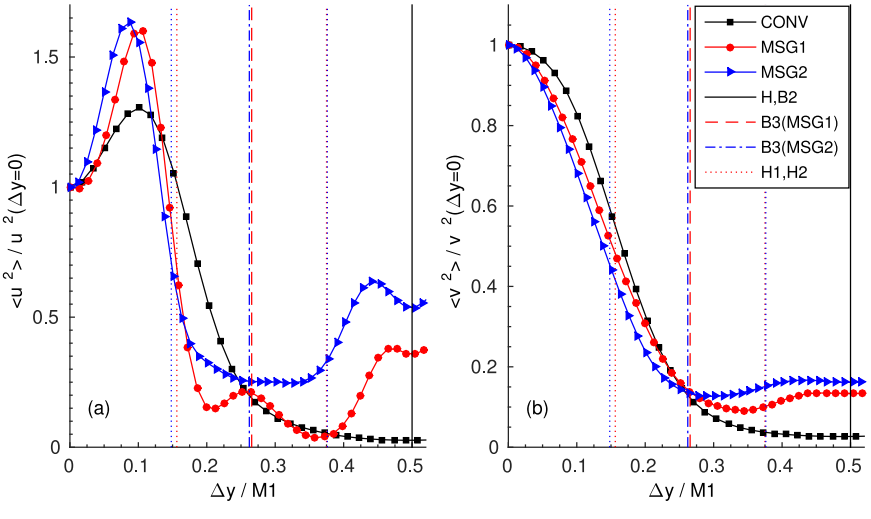

FIG. 10. The spanwise distribution of normal stresses at their peak locations behind the thickest bar B1 ($\Delta y = 0$). The distribution is symmetric about $\Delta y = 0$ and $0.5M$ (H or B2). The characteristic line positions are also marked.

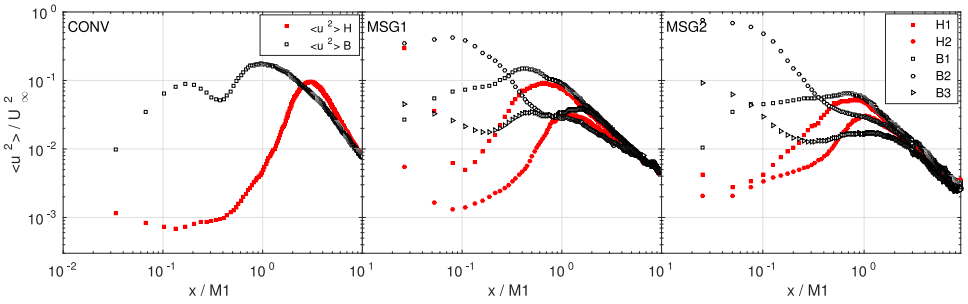

FIG. 11. Re-plot of Figure 8 in log-log scale.

It is clear from the figure that the highest $\langle v^2 \rangle$ is found along the characteristic B1 line, but the highest $\langle u^2 \rangle$ location is offset. More $\langle u^2 \rangle$ energy is found in the shear region created by the shed vortices behind B1, which is about 60% and 30% higher than at the symmetry line for the MSG and CONV grids, respectively. This vortex shedding region is also clearly shown in the vicinity of B2 of the two MSG grids (see Figure 5). Since the spatial resolution does not properly resolve the initial flow behind B3, only the MSG1 profile shows the B3 peak. At the centre of the hole ($\Delta y = 0.5M_1$), the turbulence intensity drops to a very low level for the CONV grid, which means that at $x = 1.0M_1$, the characteristic line of the hole can still be considered as part of the non-turbulent region.

The discussions of the turbulence decay rate behind grids, e.g., whether it is more exponential type or Saffman type, has not been the focus of the current work and has been discussed in details in a previous work.[20] Here Figure 8 is replotted in the log-log scale in Figure 11 to demonstrate the near-field decay behaviour behind our grids. As can be seen, a power law decay region (straight lines in log-log plots) is not yet established for any of the three grids by the end of the measurement region. Homogeneity is not strictly reached either for a sufficient streamwise distance, so that any fitted decay exponent would be very dependent on which line the fit was made for. The only conclusion that may be drawn is therefore that the flow has not reached the final stage where any of the classical theories can be said to apply.

The PIV method is also able to generate information about the turbulent kinetic energy production. The streamwise development of the two-dimensional turbulence production approximation, $\mathcal{P}_{2D}$, along the selected streamlines is shown in Figure 12. The four terms available in $\mathcal{P}_{2D}$ are

$$-\mathcal{P}_{2D} = \langle u^2 \rangle \frac{\partial U}{\partial x} + \langle uv \rangle \left(\frac{\partial U}{\partial y} + \frac{\partial V}{\partial x} \right) + \langle v^2 \rangle \frac{\partial V}{\partial y}. \tag{2}$$

The three components are denoted streamwise-, shear-, and spanwise production terms. The $\mathcal{P}_{2D}$ distributions clearly show why the flow development between the three grids are so different. For

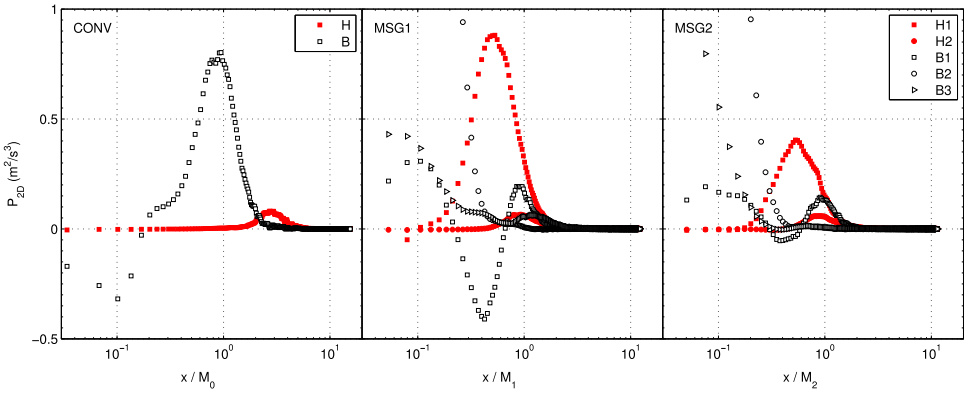

FIG. 12. The streamwise development of the 2D turbulence production $\mathcal{P}_{2D}$, behind the characteristic hole and bar locations.

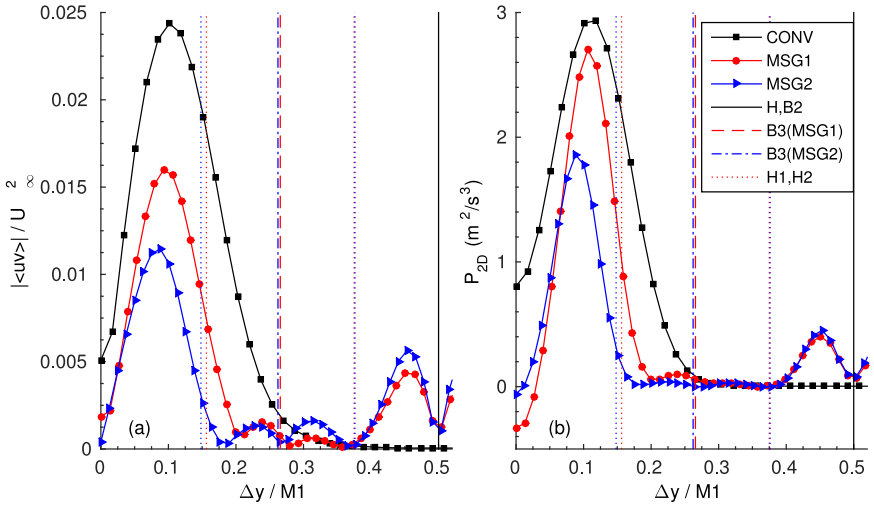

FIG. 13. Spanwise distribution of Reynolds shear stress $\langle uv \rangle$ and $\mathcal{P}_{2D}$ at the peak $\mathcal{P}_{2D}$ locations behind the thickest bar B1 ($\Delta y = 0$). (a) the magnitude of $\langle uv \rangle$ normalised by U_∞^2, in order to make direct comparison with Figures 8 and 9; (b) the absolute value of $\mathcal{P}_{2D}$. The distributions are symmetric about $\Delta y / M_1 = 0$ and 0.5.

the CONV grid nearly all the turbulent production initially occurs behind the bars. Only after $x/M_0 > 2$ is there a significant production in the hole region. For both the multi-scale grids the situation is very different, where the production in the hole region dominates except for a very short region right behind the grid.

As found for the Reynolds normal stresses, the maximum $\mathcal{P}_{2D}$ does not fall on the symmetry lines, but in the adjacent shear region (see Figure 13). This agrees with the bi-plane grid turbulence measurements of Cardesa *et al.*[4] The spanwise distributions of shear stress and $\mathcal{P}_{2D}$ are plotted in Figure 13 at the maximum $\mathcal{P}_{2D}$ magnitude along B1, i.e., $x/M_1 \approx 1.0, 0.5, 0.4$ for CONV, MSG1 and MSG2, respectively. The profiles of the shear stress and $\mathcal{P}_{2D}$ share very similar shapes, with collapsing locations of peak intensities, showing that the main contribution to $\mathcal{P}_{2D}$ comes from the shear component, even though the level of the shear stress is much lower than the normal stresses. This is because $(\partial U/\partial y + \partial V/\partial x)$ is found to be an order of magnitude larger than $\partial U/\partial x$ and $\partial V/\partial y$. Along the characteristic lines, $\mathcal{P}_{2D}$ vanishes at $x/M_1 \approx 6.4, 4.0, 3.1$ for CONV, MSG1, and MSG2, respectively (Figure 12), mainly due to the vanishing mean velocity gradients.

C. The growth of integral length scales

The longitudinal and spanwise correlation functions, f and g, are defined as

$$f\left(r_y\right) = \frac{\langle v\left(\mathbf{x}_0\right) v\left(\mathbf{x}_0 + \mathbf{e_y} r_y\right)\rangle}{\langle v^2\left(\mathbf{x}_0\right)\rangle}, \tag{3}$$

$$g\left(r_y\right) = \frac{\langle u\left(\mathbf{x}_0\right) u\left(\mathbf{x}_0 + \mathbf{e_y} r_y\right)\rangle}{\langle u^2\left(\mathbf{x}_0\right)\rangle}, \tag{4}$$

where $\mathbf{x}_0$ is the position vector, $\mathbf{e_y}$ is the spanwise unit vector and r_y the separation. Since the turbulence is highly inhomogeneous in the near field region, f and g are influenced by $\mathbf{x}_0$ to a large degree. Both f and g, as well as the integral length scale defined by the integral of f as

$$L_f = \int_0^\infty f\left(r_y\right) \mathrm{d}r_y, \tag{5}$$

were computed along all the characteristic lines.

The spanwise distributions of f and g at the locations of the peak fluctuating velocity are shown in Figure 14. Negative correlations can clearly be observed for g. The $\langle v^2 \rangle$ peak locations behind the two MSG grids are located very close to the grid, and g is strongly negative correlated

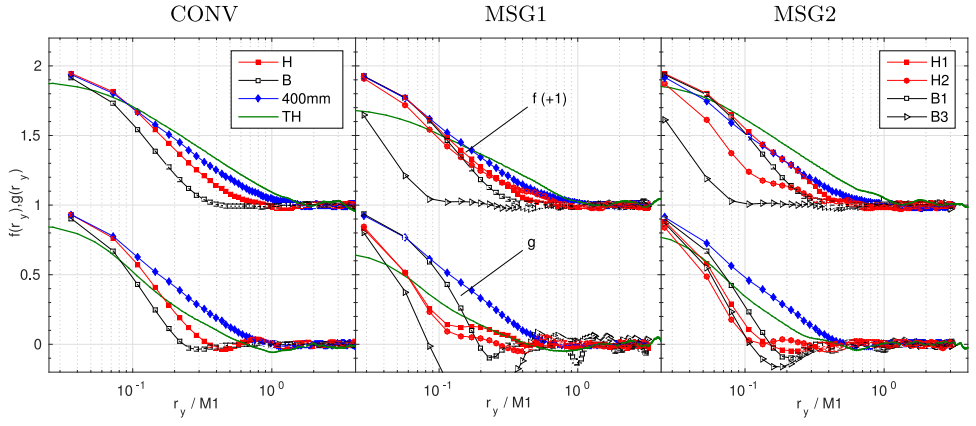

FIG. 14. The longitudinal and normal correlation functions $f(r_y)$ and $g(r_y)$ at the maximum stress location along characteristic symmetry lines, as well as at $x = 400$ mm. f and g based on the Taylor hypothesis (denoted TH) are also shown. f is shifted one unit upwards. Functions behind B2 are not presented since peaks are not clearly identified there.

here. The f and g at $x = 400$ mm ($x = 10.67M_1$ for the CONV grid) are included as typical of the far field distributions. At that location, the stresses and the PDF (not shown) of the fluctuating velocities are found to be nearly spanwise invariant.

For comparison purposes, f and g based on the Taylor hypothesis (denoted as TH) were also computed using the time-resolved data set running at 1 kHz sampling rate. In this arrangement, PIV is tantamount to a large HWA rake, and the correlation functions are computed in the conventional way used in HWA data. Therefore the TH estimated f and g separation was taken in the streamwise, rather than the spanwise direction, as opposed to the PIV f and g correlations. The computations were started at $x = 325$ mm ($x = 8.67M_1$ for CONV grid) downstream of the grid. Here the u' has dropped below 10% of the convection velocity U_∞ and the Taylor assumption of frozen equilibrium is therefore not severely violated. Figure 7 shows that for $x > 8M_1$, $U(x)$ is virtually independent of the lines followed and is very close to U_∞. It may be seen from Figure 14 that the TH estimated f loses its correlation later than the spatial f taken at $x = 400$ mm, and the TH version of g earlier than the spatial g.

The streamwise development of the integral length scale L_f calculated by Equation (5) is given in Figure 15. We have also included the TH L_f for comparison. L_f computed by TH is generally larger than the spatial ones, with the maximum excess occurring for MSG2 at about $x/M_1 = 8$. However, the order of magnitude agrees well with L_f from the spatial correlations.

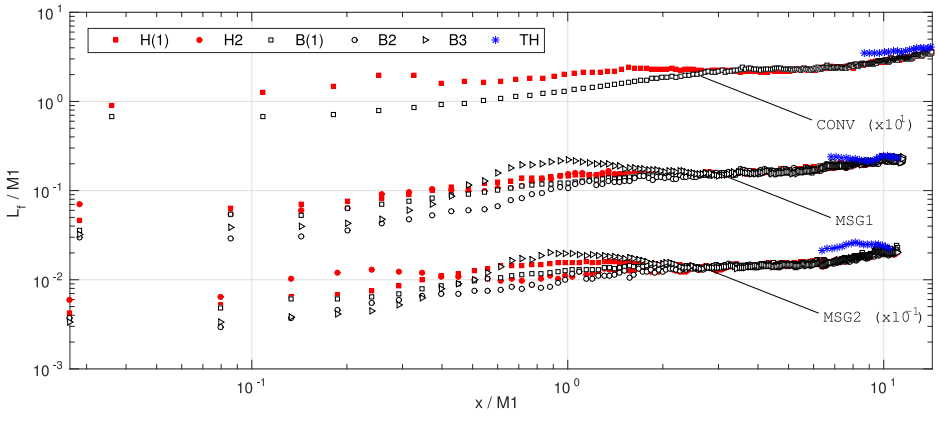

FIG. 15. The streamwise development of the integral length scale L_f defined by Equation (5), with $\mathbf{x}_0$ on all the characteristic symmetry lines. The L_f of CONV and MSG2 are shifted up and down one decade as indicated. Only every fourth data points are plotted.

After an initial development down to $x/M_1 \approx 2$, where the distribution along different lines differs significantly, L_f measured further down collapse fairly well and the growth trends for all the three grids are very similar. From $x/M_1 \approx 7$, L_f begins to show a power-law growth, as found by Krogstad and Davidson.[19] By the end of our FOV, L_f is approximately $10 - 14$ mm, with L_f behind the CONV grid being the largest.

In the initial region ($x/M_1 < 2.0$) the turbulence is rapidly developing and L_f is not always a good estimate of the large eddy size. For instance L_f along B3 is abnormally larger than along any of the other lines data with a peak at $x/M_1 \approx 1.0$. This is because geometrically B3 touches the edge of the strong shear zone behind B1 at this downstream location. Therefore L_f along B3 actually measures the thickness of the vortex sheet from B1. There, L_f is approximately twice as wide as the one from B1, which goes through the middle of this shear zone. The H1 line cuts through an inner region of the B1 wake, but L_f of MSG2 is larger than that of MSG1. This is because on the one hand the fluctuating v there is about 13% larger behind MSG1 than for MSG2 (see Figure 9). On the other hand the line from H1 in MSG1 is about 40% closer to the edge of B1 than in MSG2, so f in the former de-correlates faster than the latter.

D. Evolution of the in-plane vortices

Here the attention is shifted from the mean velocities and stresses to the measured in-plane vortices. It is known that after some initial development, the vorticity field in grid turbulence organises itself into coherent tubular structures randomly oriented in space.[8] The complete 3D information about these structures cannot be collected from the current experimental setup. Despite this limitation, some useful information from their 2D projections may be extracted with some help from conditional statistical treatments. We will focus on the region down to $x = 300$ mm from the grids (i.e., $x = 8M_1$ for CONV), before the region of few, slowly evolving vortices emerges.

The raw vorticity fields measured by the 2D PIV consist of both coherent and incoherent structures which are also locally cut by the measurement plane at unknown angles. As an example, the typical PDF of the measured ω_z at $x = 8M_1$ downstream of the CONV grid is given in Figure 16. This shows that the PDF has wider tails than the Gaussian distribution which suggests the existence of coherent structures.[31] However, the majority of the samples are at lower vorticity levels. Considering the turbulence level at this downstream distance (Figures 8 and 9), the turbulence has decayed considerably and coherent high enstrophy structures have become sparse.

This conjecture can also be qualitatively reflected from the 2D topological point of view. Chong *et al.*[6] introduced a method to classify the local eddy motion types of a turbulent flow using the velocity gradient tensor at that point. In a reduced form, the 2-by-2 velocity gradient tensors derived from two-dimensional flows[24] can also be used in a qualitative way. However, applying the local topology characterization based on 2D flow to 2D cross-sections of a 3D flow can sometimes be

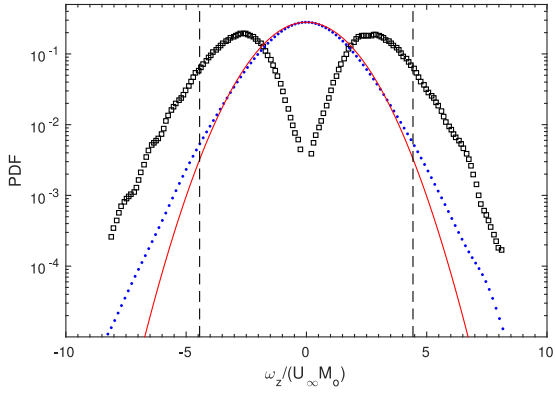

FIG. 16. The PDF of the fluctuating vorticity ω_z measured at $x = 300$ mm downstream of the CONV grid. Line $\cdots$ denotes the PDF of all the data point. $-$ is a Gaussian best fit; $\square$, the PDF of the peak ω_z; $--$ indicates the minimum ω_z value of the highest 10% population group of the peak ω_z. The plots for MSG1 and MSG2 show similar patterns.

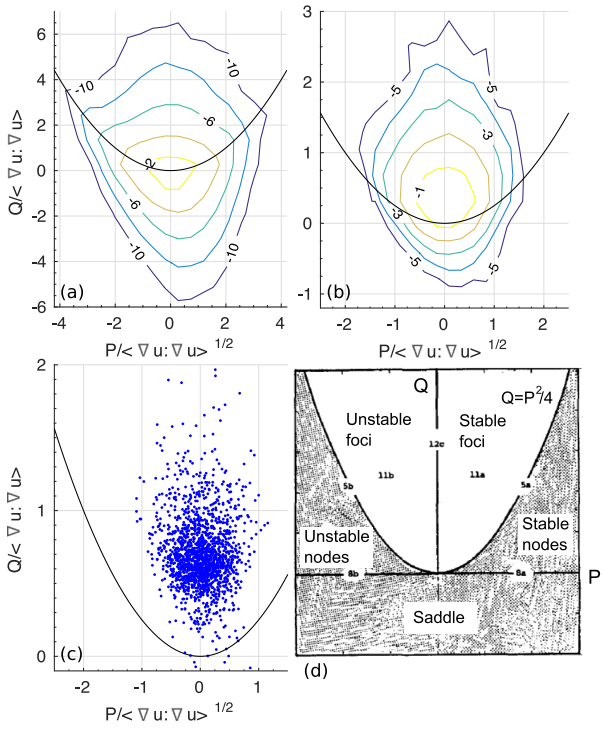

FIG. 17. The joint PDF of P and Q at $x = 300$ mm ($x = 8M_1$) downstream of the CONV grid. (a) Every ω_z data point is included; (b) the peak ω_z data points only. Contour levels in (a) and (b) are log scaled. (c) The scatter plot of the highest 10% population of the peak ω_z in (b). The plots for MSG1 and MSG2 show similar patterns. (d) Classification of critical points on the P-Q chart; see the work of Perry and Chong[24] or Chong *et al.*[6] for details.

misleading, as pointed out by the same authors.[25] Since the orientation of the 2D sections has influences on the *interpreted* classification, it will be shown that the problem related to large cutting angles can be reduced for some selected ω_z.

The reduced 2-by-2 velocity gradient tensor of a fully 3D flow is written as

$$\nabla\mathbf{u}(\text{reduced}) = \begin{bmatrix} \dfrac{\partial u}{\partial x} & \dfrac{\partial u}{\partial y} \\ \dfrac{\partial v}{\partial x} & \dfrac{\partial v}{\partial y} \end{bmatrix} \tag{6}$$

and is available from our measurement. The two invariants of $\nabla\mathbf{u}$ are $P = -trace\,(\nabla\mathbf{u})$ and $Q = det\,(\nabla\mathbf{u})$. The location of a flow particle in the $P-Q$ plot provides the *apparent* information of its type of motion instantaneously, e.g., the parabolic curve $Q = P^2/4$ separates the foci and nodes in the positive half of Q[24] shown in Figure 17(d).

Using CONV grid data as example, the joint $P-Q$ PDF of all the fluctuating vorticity ω_z data at $x = 8M_1$ are shown in Figure 17(a). The P,Q axes are normalised by the mean tensor double dot product $\langle\nabla\mathbf{u} : \nabla\mathbf{u}\rangle$. It can be seen that the distribution is weakly skewed towards the second and fourth quadrants. It has been shown that in a fully developed incompressible homogeneous 3D turbulent flow, an arbitrary 2D section cut displays a clear skewing[5] with $\langle PQ\rangle < 0$. Under similar spatial resolution, in Figures 17(a) $\langle PQ\rangle / \langle\nabla u : \nabla u\rangle^{3/2} \approx -0.076$. Not surprisingly, in addition to the foci type population, either stable or unstable, a large saddle type of population and a small nodes type of population are also present. This means that the incoherent vorticity *appeared* to form up a large proportion of the measured ω_z.

In order to isolate the higher intensity ω_z which are most likely associated with coherent structures,[31] we propose an approach which consists of two steps. First, in every snapshot of the ω_z field, the regional highest $|\omega_z|$ is selected. This regional peak search is conducted from $x = 1M_1$ downstream of the grids onwards in a step of $\Delta x = 0.5M_1$. The regional search area has a size of

$\pm 0.5M_1$ and ± 4 data points in the spanwise and streamwise directions, respectively, and are centred behind the thickest bar B1. This searching area ensures higher chances to pick out the highest local $|\omega_z|$, while maintaining a sufficient sample size. The process filters out 95% of the data points and a typical PDF of the remaining ω_z sample is shown by the square symbols in Figure 16. It shows that most of the low $|\omega_z|$ points have been excluded. The effect in terms of topology is immediate. Compared with Figure 17(a), Figure 17(b) shows a clear positive Q shift of the population centre, with a noticeable shrinking of saddle and node areas. The data points in these areas could also originate from tube-like structures whose structure axis locally cuts the measurement plane at a large angle θ.[25] Here θ is defined as the angle between the vortex axis and the measurement plane perpendicular direction (e.g., $\theta = 0$ for cut normal to the structure axis). Therefore, by reducing the population in these regions, we also reduce the counts of data points which could be tube like but have large θs.

The second step involves further selecting the highest 10% of $|\omega_z|$ among the population remaining after the first step at each downstream station, which reduces the sample size further to about 0.5% of the original data. Figure 17(c) shows that nearly all the points have foci characteristics, i.e., in the region surrounded by $Q = P^2/4$. The procedure from Figures 17(a) to 17(c) suggests that the very strongest 0.5% of the vorticity consists of structures which appear to be tube-like when cut by the measurement plane, with some being stretched and some being contracted locally.

The first available quantity which can be derived from a conditional averaging process centering on these selected vortices, is the mean vortex size. This is obtained from the 2D cross-correlation function $h(\mathbf{r})$ of the ω_z field

$$h(\mathbf{r}) = \frac{\langle \omega(\mathbf{r}_0)\,\omega(\mathbf{r}_0 + \mathbf{r})\rangle}{\langle \omega^2(\mathbf{r}_0)\rangle}. \tag{7}$$

The function $h(\mathbf{r})$ shows a nearly Gaussian distribution as early as $1M_1$ downstream of the grids. Figure 18(a) presents $h(\mathbf{r})$ along the streamwise and spanwise directions, as well as along the diagonal, as function of the downstream distances. Although there are some differences among the three directions, a common characteristic is that $h(\mathbf{r})$ remains Gaussian in the bulk part, but has

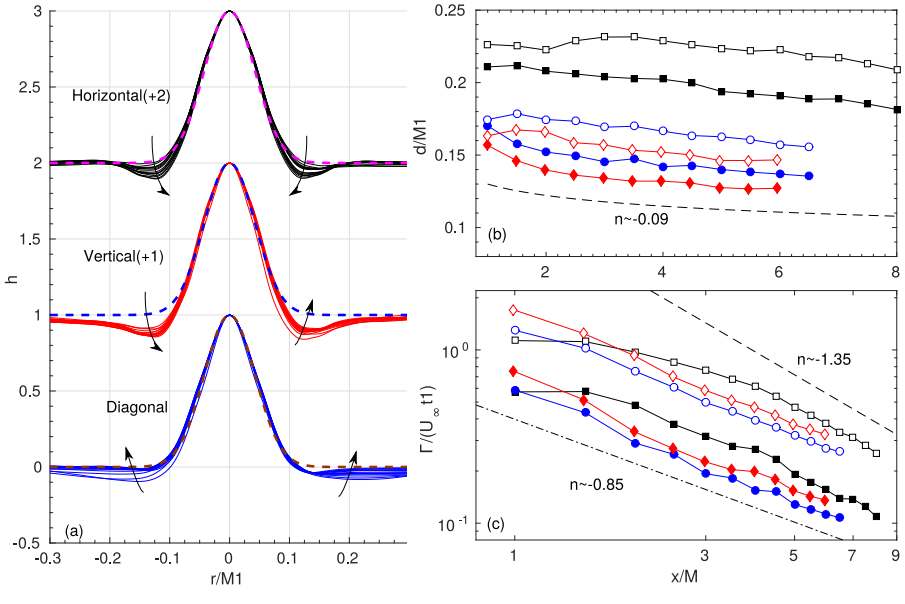

FIG. 18. (a) The ω_z correlation function h conditionally averaged at the peak ω_z centres for the CONV grid. The correlation functions along the streamwise and spanwise directions are shifted. Lines −− denote the best Gaussian fits and the arrows indicate the development of the function in the streamwise direction. (b) The evolution of the measured averaged vortex size as a function of the downstream distances x. Filled symbols for peak ω_z; open symbols for the highest 10% of the peak population. □ for CONV, ○ for MSG1, ◇ for MSG2. −− indicates the power law trend $x^{-0.09}$. (c) The measured Γ evolution normalised by the thickest bar size t1 and U_∞. Symbols as in (b). Lines −− and − · − are $x^{-1.35}$ and $x^{-0.85}$.

negative tails at larger r. Using the separation r where $h(\mathbf{r})$ crosses zero to estimate the in-plane vortex size, the evolution of the vortex diameter d for all the three grids, averaging along the three directions, is shown in Figure 18(b). The vortex size behind the CONV grid is consistently ~0.5 mm larger than for the MSG grids, a consequence of introducing the multiple length scales of the MSG grids. The decay rate of d after $x = 4M_1$ is fairly weak, with the CONV grid decay rate being slightly faster. A power law $d \sim x^{-0.09}$ is a good fit to this range for all the grids.

The second quantity that can be calculated from the vortex data is the projected circulation Γ in the measurement plane, as a measure of the local vortex strength,

$$\Gamma = \oint_c \mathbf{u}_{2D} \cdot \mathrm{d}\mathbf{c} = \int_S \omega_z \cdot \mathrm{ds}, \tag{8}$$

where c and S are the circumference and the area of the positively correlated region. This is shown in Figure 18(c). The decay of Γ behind the CONV grid starts at a slower rate compared to the MSG grids, but picks up to a faster one for $x > 3M_1$. The difference between the grids is clear towards the end of the measurement range, e.g., $4 < x/M_1 < 7$. A power law fit for this range suggests decay rate exponents between $n \sim -1.35$ and -0.85. Again it would have been useful to have more data further downstream to see if the decay rates for the three grids collapse in the far field.

The data also provide information about the early development of the strain and the rotational components of the 2D part of $\nabla\mathbf{u}$,

$$S_{ij} = \frac{1}{2}\left[\nabla\mathbf{u} + (\nabla\mathbf{u})^T\right], \tag{9}$$

$$R_{ij} = \frac{1}{2}\left[\nabla\mathbf{u} - (\nabla\mathbf{u})^T\right], \tag{10}$$

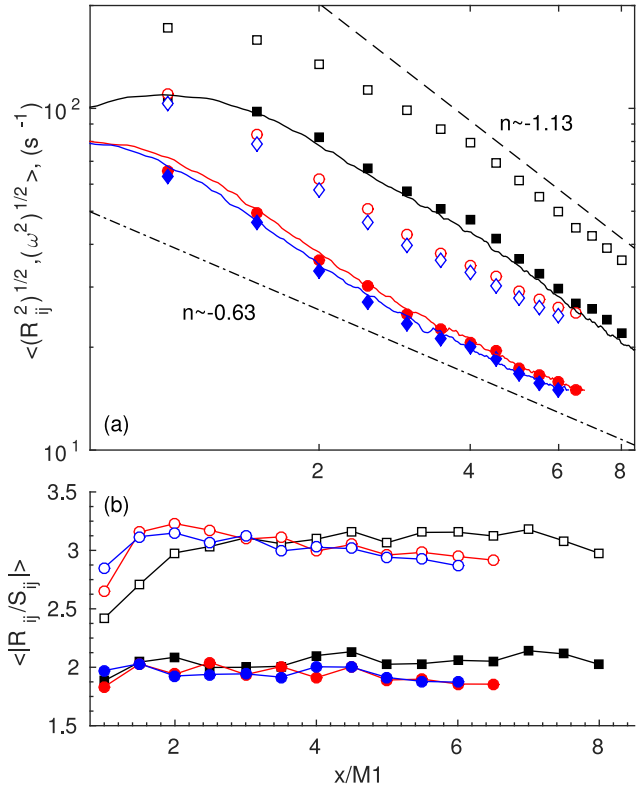

FIG. 19. (a) The near-field evolution of the mean vorticity $\left\langle (\omega^2)^{1/2} \right\rangle$ and the mean rotation rate $\left\langle \left(R_{ij}^2\right)^{1/2} \right\rangle$. Symbols as in Figure 18(b) and solid lines – denote the mean vorticity of every measurement point. The reference line –– and –·– denote x^n with power n −1.13 and −0.63 respectively. (b) The evolution of eccentricity (the ratio of the mean rotation rate magnitude $\langle |R_{ij}| \rangle$ to the mean strain rate $\langle |S_{ij}| \rangle$ at peak vorticity points); symbol notations follow Figure 18(b).

at the vortex centre, shown in Figure 19(a). Not surprisingly, the early interaction of multiple length scales leads to a weaker R_{ij} of the MSGs than behind the CONV grid. As found for Γ, the MSG grids have a faster initial decay followed by a slower one after $4M_1$. A power law fit suggests an exponent between $n = -1.13$ and -0.63 for $x > 4M_1$ near the end of the range examined. Since on average, $h(\mathbf{r})$ is nearly Gaussian, Γ can be written as $2\pi \int_0^{r(h=0)} r\omega_z h(r)\,\mathrm{d}r$. Combining the decay rates of d and Γ in Figures 18(b) and 18(c), it can be deduced that $h(r)$, up to the zero-crossing r, is a very weak function of x.

Figure 19(b) shows the evolution of the ratio $\langle |R_{ij}/S_{ij}| \rangle$ at the vortex centres, as a quantification of their *relative* rotational strength and hence how strong the vortex is deformed under the external strain field. The ratio is shown to be larger than unity over the entire observation range, lending support to the efficiency of the vortex selection steps described above. The trend of the solid symbols containing the peak values only is not as clear as the open symbols, which represent the highest 10% population. All grids (open symbols) display an initial increase of $\langle |R_{ij}/S_{ij}| \rangle$ followed by a weak decay. The fact that the distribution for the highest 10% population for the CONV grid initially has lower $\langle |R_{ij}/S_{ij}| \rangle$ than the multi-scale grids implies stronger relative deformation effects than for the multiple length scale cases for $x/M_1 < 3$, another example of differences in the evolution of conventional and multi-scale grid wakes in the near grid region.

IV. CONCLUSION

This paper reports some results from a 2D PIV study of turbulence in the immediate vicinity of three mono-plane grids. One is a conventional grid with square holes, and two consist of multiple length scales. The velocity field is measured using four stitched cameras sampled at statistically independent field of views. The measurements are conducted in a plane cutting through the centre of holes. Compared to the conventional grid, which exhibits two symmetry lines, the two multi-scale grids MSG1 and MSG2 have five characteristic symmetry lines in the measurement plane each and the flow structures are found to be very complex.

From the mean velocity and turbulence quantities along these characteristic lines it is found that for all three grids, the mean velocity becomes approximately homogeneous after about six times the largest mesh scale. The turbulence quantities need more than $10M_1$ downstream to be uniform[20] (M_1 being the largest scale of a grid geometry). The integral length scale L_f obtained by integrating the spanwise velocity component longitudinal correlation function, reflects the multiple length scales in the MSG grids. The L_f along the characteristic symmetry lines along which the distribution was followed showed individual development before they all collapsed after about $3M_1$. No clear difference was observed in terms of the growth rates among the three grids after that. The various length scales associated with the grid geometry have lost their impact on the flow well before the turbulence becomes homogeneous.

While the mean and integral quantities do not show clear differences among the three grids after an initial development ($x < 4M_1$), the differences become clear in terms of the decay rates of peak vorticity magnitude and sectional vortex circulation when examining the individual coherent vortices. The different decay rates reflect the effect of multiple length scales introduced at the mesh. Despite the different decay rates, the averaged in-plane vortex structure shapes are shown to be similar, remaining near Gaussian, and do not change much over the examined range. Although the distributions are seen to merge downstream, the streamwise extent of the examined flow is too short to say if the observed differences extend to the far field.

Note that the current study concentrates on the near-field wake flow only. The extent of our FOV is not sufficient to draw a conclusion on the turbulence energy decay rate. As shown in Figure 11, although a power-law decay seems to exist at the very end of the data range, the extent of the linear part is not sufficiently long for a reliable fit to be made. Moreover, even though the flow has become almost spanwise homogeneous at our most downstream measurement point, the flow is not fully developed in the sense of a balance between the decay of kinetic energy and local dissipation rate.

A peculiarity of the flow immediately behind the bars of the mono-plane CONV grid is that it lacks the recirculation zone commonly observed behind normal facing obstacles and have been reported in bi-plane grid wakes. Our RANS modelling results confirmed the absence of recirculation at the measurement plane through the centre of the grid holes and verifies that this was not a measurement resolution problem. The RANS data showed that this is due to the very strong reversed flow at the bar crosses, which sucks in fluid from all sides, including sideways along the bars, forming a saddle point flow type behaviour half-way down the bars. This suggests that there exists a critical bar width, or a critical blockage ratio, smaller than the 44% in the present grid, below which a recirculation zone will appear as the influence of the bar crosses on the local flow further along the bar decreases. This confirms earlier findings that the grid solidity should not be much higher than 45% before the flow through the holes start to interact strongly and delay the development towards spanwise homogeneity. The limiting case is of course a single bar wake when the grid blockage ratio $\sigma \to 0$.

ACKNOWLEDGMENTS

The authors would like to thank Mr. Dhiren Mistry in helping with the experimental setup at the Engineering Department, University of Cambridge and Dr. Jose I. Cardesa-Dueñas for valuable discussions.

[1] G. K. Batchelor, *The Theory of Homogeneous Turbulence* (Cambridge University Press, Cambridge, UK, 1953).
[2] L. H. Benedict and R. D. Gould, "Towards better uncertainty estimates for turbulence statistics," Exp. Fluids **22**, 129–236 (1996).
[3] J. C. Bennett and S. Corrsin, "Small Reynolds number nearly isotropic turbulence in a straight duct and a contraction," Phys. Fluids **21**, 2129–2140 (1978).
[4] J. I. Cardesa, T. B. Nickels, and J. R. Dawson, "2D PIV measurements in the near field of grid turbulence using stitched fields from multiple cameras," Exp. Fluids **52**(6), 1611–1627 (2012).
[5] J. I. Cardesa, D. Mistry, L. Gan, and J. R. Dawson, "Invariants of the reduced velocity gradient tensor in turbulent flows," J. Fluid Mech. **716**, 597–615 (2013).
[6] M. S. Chong, A. E. Perry, and B. J. Cantwell, "A general classification of three-dimensional flow fields," Phys. Fluids A **2**, 765–777 (1990).
[7] S. Corrsin, "Turbulence: Experimental methods," Handb. Phys. **8**, 524–533 (1963).
[8] L. Djenidi, "Lattice-Boltzmann simulation of grid-generated turbulence," J. Fluid Mech. **552**, 13–35 (2006).
[9] T. A. Earl, L. Thomas, S. Cochard, R. B. Salah, B. Tremblais, and L. David, "Volumetric measurements by tomographic PIV of grid generated turbulence in an open channel flow," in Eighth International Symposium on Turbulence and Shear Flow Phenomena, Poitiers, France (2013).
[10] O. Ertunç, N. Özyilmaz, H. Lienhart, F. Durst, and K. Beronov, "Homogeneity of turbulence generated by static-grid structures," J. Fluid Mech. **654**, 473–500 (2010).
[11] W. K. George and H. Wang, "The exponential decay of homogeneous turbulence," Phys. Fluids **21**, 025108 (2009).
[12] R. Gomes-Fernandes, B. Ganapathisubramani, and J. C. Vassilicos, "Particle image velocimetry study of fractal-generated turbulence," J. Fluid Mech. **711**, 306–336 (2012).
[13] R. Gomes-Fernandes, B. Ganapathisubramani, and J. C. Vassilicos, "Evolution of the velocity-gradient tensor in a spatially developing turbulent flow," J. Fluid Mech. **756**, 252–292 (2014).
[14] R. Gomes-Fernandes, B. Ganapathisubramani, and J. C. Vassilicos, "The energy cascade in near-field non-homogeneous non-isotropic turbulence," J. Fluid Mech. **771**, 676–705 (2014).
[15] R. J. Hearst and P. Lavoie, "Decay of turbulence generated by a square-fractal-element grid," J. Fluid Mech. **741**, 567–584 (2014).
[16] D. Hurst and J. C. Vassilicos, "Scalings and decay of fractal-generated turbulence," Phys. Fluids **19**, 035103 (2007).
[17] Jayesh and Z. Warhaft, "Probability distribution, conditional dissipation, and transport of passive temperature fluctuations in grid-generated turbulence," Phys. Fluids **4**, 2292–2307 (1992).
[18] P.-Å. Krogstad and P. Davidson, "Freely-decaying, homogeneous turbulence generated by multi-scale grids," J. Fluid Mech. **680**, 417 (2011).
[19] P.-Å. Krogstad and P. A. Davidson, "Is grid turbulence Saffman turbulence?," J. Fluid Mech. **642**, 373–394 (2010).
[20] P.-Å. Krogstad and P. A. Davidson, "Near-field investigation of turbulence produced by multi-scale grids," Phys. Fluids **24**, 035103 (2012).
[21] P. Lavoie, L. Djenidi, and R. A. Antonia, "Effects of initial conditions in decaying turbulence generated by passive grids," J. Fluid Mech. **585**, 395–420 (2007).
[22] K. Nagata, H. Suzuki, Y. Sakai, T. Hayase, and T. Kubo, "Direct numerical simulation of turbulent mixing in grid-generated turbulence," Phys. Scr. **T132**, 014054 (2008).
[23] H. Norbach, "Influence of individual variations of particle image intensities on high-resolution PIV," Exp. Fluids **50**(4), 919–927 (2011).
[24] A. E. Perry and M. S. Chong, "A description of Eddy motions and flow patterns using critical-point concepts," Ann. Rev. Fluid Mech. **19**, 125–155 (1987).

[25] A. E. Perry and M. S. Chong, "Topology of flow patterns in vortex motions and turbulence," Appl. Sci. Res. **53**, 357–374 (1994).
[26] P. J. Saffman, "The large-scale structure of homogeneous turbulence," J. Fluid Mech. **27**, 581 (1967).
[27] L. F. G. Simmons and C. Salter, "Experimental investigation and analysis of the velocity variations in turbulent flows," Proc. R. Soc. London, Ser. A **145**, 212–234 (1934), Containing Papers of a Mathematical and Physical Character.
[28] A. Thormann and C. Meneveau, "Decay of homogenous, nearly isotropic turbulence behind active fractal grids," Phys. Fluids **26**, 025112 (2014).
[29] W. S. J. Uijttewaal and G. H. Jirka, "Grid turbulence in shallow flows," J. Fluid Mech. **489**, 325–344 (2003).
[30] D. C. Wilcox, *Turbulence Modeling for CFD*, 3rd ed. (DCW Industries, 2006).
[31] M. Wilczec, B. Kadoch, K. Schneider, R. Friedrich, and M. Farge, "Conditional vorticity budget of coherent and incoherent flow contributions in fully developed homogeneous isotropic turbulence," Phys. Fluids **24**, 035108 (2012).